Semi-coupling of a Field-scale Resolving Land-surface Model and WRF-LES to Investigate the Influence of Land-surface Heterogeneity on Cloud Development

Jason S. Simon[1], Andrew D. Bragg[1], Paul A. Dirmeyer[2], and Nathaniel W. Chaney[1]

[1]Duke University
[2]George Mason University

Key Points:

- Large-eddy simulation is used to study fine-scale heterogeneity in land-atmosphere coupling
- Spatial patterns of dry and wet areas increase cloud production via mesoscale circulations
- Sub-grid scale heterogeneity should ideally be included in global model parameterizations

Corresponding author: Jason Simon, jason.simon@duke.edu

Abstract

Contemporary Earth system models mostly ignore the sub-grid scale (SGS) heterogeneous coupling between the land surface and atmosphere, to a detriment that remains largely unknown. To both evaluate the effect of SGS heterogeneity for realistic scenarios and aid in the development of coupled land and atmosphere SGS parameterizations for global models, we present a study of the effect of sub-100 km scale land-surface heterogeneity on cloud development. In the primary experiment we use the Weather Research and Forecasting (WRF) model to conduct two large-eddy simulations over the Southern Great Plains (SGP) site using 100-m horizontal resolution on a domain that spans 100 km in each lateral direction. The first simulation uses high-resolution land-surface fields specified by an offline land-surface model (LSM), while the second uses homogenized land-surface fields found by taking a domain-averaged value of each field at each timestep. The atmospheric development of the heterogeneous and homogeneous simulations are compared, primarily in terms of cloud production and turbulent kinetic energy. It is seen that the heterogeneous case develops a mesoscale circulation pattern which generates additional clouds and turbulence compared to the homogeneous case. Additional experiments isolate sources of heterogeneity in the LSM (including forcing meteorology) to better understand relevant land-surface processes, and modify the Bowen ratio and initial wind profile of the heterogeneous case to clarify the results seen. Finally two additional days at the SGP site are simulated confirming the increase in cloud production in heterogeneous cases.

Plain Language Summary

A modern Earth system model combines an atmospheric model and land-surface model, and the two interact during a simulation. Due to computational constraints, global models today use grids where very large areas (sometimes in excess of 10,000 square kilometers) are represented by a single point, making it impossible to directly represent many important features, particularly those related to the development of clouds and rain. Approximations of these processes that cannot be represented are included by simpler submodels called parameterizations, which often base calculations on average values over the area they are modeling. To aid in the improvement of these parameterizations, a high-resolution model (where each point represents only 0.01 square kilometers) is used to simulate three summer days in Oklahoma over a total area of 10,000 square kilometers. It is seen that simulations where the land surface has moist and dry patches from previous rain events produce more clouds than simulations where the same amount of soil moisture is evenly distributed over the entire surface. We hope that this and future work will both motivate and aid efforts to add considerations for the spatial distribution of features, in addition to their average, to the parameterizations used in Earth system models.

1 Introduction

A critical challenge in characterizing land-atmosphere interactions across scales in Earth system models (ESMs) is the non-linearity that emerges as a result of spatial heterogeneities over land (e.g., land use and topography) (Albertson et al., 2001; Bou-Zeid et al., 2004; Huang & Margulis, 2013; Shao et al., 2013; Clark et al., 2015). These complex interactions between the land-surface processes and the underlying physical environment drive the spatial complexity of surface fluxes and states (Western et al., 1999; Gómez-Plaza et al., 2001; Jacobs et al., 2004; Chaney et al., 2015). As a result, the macroscale behavior of the water and energy cycles cannot be disentangled from their fine-scale processes and interactions. The heterogeneities that emerge over land, in turn, can play a key role in many important atmospheric processes, such as setting the atmospheric boundary layer (ABL) depth, initiating convection, and spawning mesoscale circulations (Ntelekos

et al., 2008; Kustas & Albertson, 2003; Timmermans et al., 2008; Bertoldi et al., 2013; Gutowski et al., 2020). Although progress is being made in understanding the role of multi-scale land heterogeneity on microscale and mesoscale meteorological processes in regional and local studies (Kustas & Albertson, 2003; Talbot et al., 2012; Bertoldi et al., 2013; Huang & Margulis, 2013; Shrestha et al., 2014; Senatore et al., 2015), its role in land-atmosphere interactions in the climate system as a whole remains mostly unknown. This is primarily due to the over-simplistic coupling between existing sub-grid parameterizations in land surface models and atmospheric models (e.g., tiling schemes, Ducharne et al., 2000; Bonan et al., 2002; Milly et al., 2014; Chaney et al., 2018; Lawrence et al., 2019). Existing ESMs only exchange sub-grid spatial mean fluxes of mass and energy between the land and atmosphere while disregarding higher order sub-grid spatial statistics (e.g., spatial variance). Convection and turbulence parameterizations in atmospheric circulation models are moving towards the inclusion of higher-order SGS processes (e.g., Cloud Layers Unified By Binormals (CLUBB) and Eddy Diffusivity Mass Flux (EDMF), Golaz et al., 2002; Sušelj et al., 2013), providing an opportunity for potential coupling with the SGS heterogeneity of the land surface.

There have been many modeling studies on heterogeneous land surfaces and their effects on atmospheric dynamics, primarily using idealized surface flux fields and initial atmospheres. Pielke Sr (2001) gives a very thorough theoretical background and review of work done studying the effect of heterogeneous spatial distributions of sensible and latent heat fluxes from the land surface on the development of cumulus convective rainfall in the atmosphere. Notably, Avissar and Schmidt (1998) studied the influence of heterogeneity in the surface sensible heat flux field in a dry atmosphere using a large-eddy simulation (LES), finding that the scale of the surface heat flux does influence the development of the atmospheric boundary layer (ABL) in the absence of a mean wind, but that the effects of the surface heterogeneity are "virtually eliminated" by a background wind of 5 m s^{-1}. They also found that the presence of moisture combined with heterogeneous fluxes could lead to pockets of moisture which may lead to cloud development which would not be present in a homogeneous case. They finally concluded that for heterogeneity of scales smaller than 5 – 10 km, a mean flux value over a grid cell may be used without affecting the CBL development, even with no background wind present. A modeling study by Findell and Eltahir (2003), using a nested mesoscale framework with uniform surface moisture, found that the influence of the background wind on surface fluxes, as it relates to triggering convection, is more nuanced, and can either suppress or enhance convection depending on the direction and amount of shear. More recently, Kang (2016) conducted an LES study of scales of surface-flux heterogeneity, finding that surface-flux fields with large Bowen ratios and large scales of heterogeneity are able to trigger deep convection, where more homogeneous cases are not. Kang (2020) conducted a similar LES study with multiple degrees of heterogeneity in the surface-flux fields finding that heterogeneous surface fields reduced the decay of turbulent kinetic energy (TKE) in the atmosphere.

Heterogeneous surface fields have also been studied observationally, often with noted differences from modeling studies. Taylor et al. (2011) used satellite observations to study the influence of soil moisture on the development of convective rain storms in West Africa, concluding that soil moisture variations at $\mathcal{O}(10 - 40$ km) strongly control storm development in the region. Taylor et al. (2012) studied the feedback mechanisms between soil moisture and convective storms from global observations, finding that drier soils are more likely to produce afternoon rainfall events while wetter soils show no preference for rain development. They note that this result is in contrast to many weather and climate models, which show a preference for rainfall development over wetter soils. Phillips and Klein (2014) studied the Southern Great Plains (SGP) site and found that, while large-scale forcings tend to dominate, there are some cases where local feedbacks from the surface play a role in the atmosphere, particularly as soil dries after a precipitation event. They

also note a contrast between their results and modeling efforts, where models tend to over-predict a coupling between soil moisture and precipitation.

To aid in the development of an effective sub-grid coupling between the modeled land-surface and atmospheric heterogeneity in ESMs, more must be known about the impact of land-surface heterogeneity on atmospheric dynamics. To this end, the study presented here uses output from HydroBlocks, a field-scale resolving land-surface model (LSM), to drive the surface of the Weather Research and Forecasting (WRF) model, run in LES mode, over the SGP site using initial profiles and large-scale temperature and moisture fluxes based on observations. The result is a realistic study on the coupling between the land surface and ABL development over a diurnal cycle, with a specific interest in the role of land-surface heterogeneity on cloud production. A domain area of 100 km $\times$ 100 km is used, which allows domain-wide mean values to be taken as a representation of a grid-scale value in a global model and the effects of land-surface heterogeneity, which would be SGS on a climate-scale grid, on the grid-scale signal to be studied directly via LES. With this study, we aim to help to answer three questions which are key to the development of global-scale parameterizations which consider SGS heterogeneity. First, are the effects of land-surface heterogeneity which are seen in more idealized LES studies, specifically emergent mesoscale circulations between wet and dry areas, observed when using realistic surface flux fields? Second, what is the impact on the macroscale (domain-wide) signal of the heterogeneous land surfaces? Finally, what is the relative impact of the different sources of heterogeneity in the LSM (e.g., soil type, rivers and surface water, soil moisture, etc.)?

The primary experiment here is a pair of simulations of September 24, 2017: the first simulation uses the high-resolution HydroBlocks land surface while the second spatially homogenizes the land surface by using domain-averaged values at each grid point (Sec. 3.1). Cases are then considered where only certain land-surface features are represented heterogeneously in the driving HydroBlocks simulation, generating different scales of surface heterogeneity (Sec. 3.2). Additional cases are also considered by modifying the heterogeneous case so that the Bowen ratio at the surface is increased, and the initial wind profile is adjusted (Sec. 3.3). Finally, the primary heterogeneous vs. homogeneous experiment is repeated for simulations of June 10, 2016 and July 16, 2017 and are analyzed briefly (Sec. 3.4).

2 Model description

2.1 WRF

Atmospheric simulations are conducted using version 3.8.1 of the WRF model (Skamarock et al., 2008) as an LES (WRF-LES). Model settings largely follow those used in the LES ARM Symbiotic Simulation and Observation Workflow (LASSO) campaign (W. Gustafson et al., 2019; W. I. Gustafson et al., 2020), which is publicly-available dataset of LES cases over the SGP site. The key difference between the LASSO simulations and those presented here is the specification of heterogeneous surface conditions. The LASSO simulations use spatially-uniform, time-evolving surface fields for sensible heat flux, latent heat flux, and skin temperature (specified directly), as well as a spatially-uniform and constant momentum roughness. Here, heterogeneous cases use two-dimensional, time-evolving surface fields for sensible heat flux, latent heat flux, skin temperature (found via specified emissivity and upward longwave radiation fields), albedo, and momentum roughness, all obtained from the HydroBlocks LSM described in Sec. 2.2. The surface fields from the HydroBlocks LSM are semi-coupled to the atmosphere in the WRF model, i.e., the LSM is run offline using reanalysis meteorology, and there is no feedback from the atmosphere to the land surface in the LES. Other notable differences between the WRF settings used here and those used by LASSO are the expansion of the domain to 100 km $\times$ 100 km (where the LASSO domain is 25 km $\times$ 25 km), the use of the isotropic

three-dimensional Smagorinsky-Lilly turbulence closure model (where LASSO uses the isotropic three-dimensional Deardorff model), and the inclusion of a Coriolis forcing (where LASSO considers every grid point to be at the same latitude and longitude).

Following the LASSO configuration, simulations use the Thompson graupel microphysics scheme and the RRTMG radiation scheme (though surfaces are specified offline by HydroBlocks) with the cumulus and PBL schemes turned off. The horizontal resolution is $\Delta_{x,y} = 100$ m with a timestep of 0.5 s. The domain is approximately 14.5 km tall with 227 vertical levels and a vertical resolution of $\Delta_z = 30$ m in the lower 5 km of the column. Periodic boundary conditions are used in both lateral directions and a w-Rayleigh damping layer is applied in the upper 2 km of the column. The LES domain uses a flat bottom boundary, though terrain is considered by the offline HydroBlocks simulation for surface routing. Initial profiles for potential temperature, water vapor mixing ratio, and lateral velocity components are obtained from the LASSO database and are applied uniformly to the domain. A relatively unique feature of the LASSO simulations is the inclusion of large-scale heat and moisture flux profiles that are applied uniformly on every column in the grid at each timestep, allowing the use of a single non-nested domain while still providing considerations for large-scale meteorology. Forcing data for these large-scale fluxes are also obtained from the LASSO database.

2.2 HydroBlocks

HydroBlocks is a field-scale resolving land-surface model (Chaney, Metcalfe, & Wood, 2016) that accounts for the water, energy, and carbon balance to solve land-surface processes at high spatial and temporal resolutions. HydroBlocks leverages the repeating patterns that exist over the landscape (i.e., the spatial organization) by clustering areas of assumed similar hydrologic behaviour into hydrologic response units (HRUs). The simulation of these HRUs and their spatial interactions allows the modeling of the water and energy cycles at field scales (30 m) over regional to continental extents (Chaney, Metcalfe, & Wood, 2016; Chaney et al., 2020; Vergopolan et al., 2020). The core of HydroBlocks is the Noah-MP vertical land surface scheme (Niu et al., 2011). HydroBlocks applies Noah-MP in an HRU framework to explicitly represent the spatial heterogeneity of surface processes down to field scale. At each timestep, the land-surface scheme updates the hydrological states at each HRU; and the HRUs dynamically interact laterally via subsurface flow.

For this study, HydroBlocks is spun up for two years and uses high-resolution (30 m) soil type and land cover maps from the Probabilistic Remapping of SSURGO (POLARIS) (Chaney, Wood, et al., 2016; Chaney et al., 2019) and National Land Cover Database (NLCD) (Homer et al., 2012) datasets, respectively, and one-eighth degree NLDAS-2 meteorology (Cosgrove et al., 2003; Mitchell et al., 2004) with NCEP Stage-IV radar rainfall (∼4 km) data (Lin & Mitchell, 2005). The hourly state of the land surface produced by HydroBlocks for the period of interest is then used to specify surface values in the WRF model for: sensible heat flux, latent heat flux, momentum roughness coefficient, albedo, emissivity, and upward longwave radiation. Surface skin temperature is then diagnosed from emissivity and upward longwave radiation, and homogenized skin temperature is similarly diagnosed from homogenized upward longwave radiation and homogenized emissivity (rather than a domain-average of skin temperature directly). For consistency, surface-flux fields are adjusted so that the domain-wide averages match the time-evolving scalar surface fluxes specified by the LASSO campaign, which are from the observationally-improved VARANAL dataset.

3 Results

Simulations are performed on a 100 km × 100 km domain over the SGP site, centered at 36.6° N, 97.5° W. The domain is largely cultivated cropland and grassland, with

a few small urban areas and a tributary of the Arkansas River running primarily west-east through the domain (Fig. 1). The basic heterogeneous and homogeneous cases are the primary experiment, and the additional experiments are used to clarify the results seen in the primary experiment. Comparisons between cases are made primarily by evaluating the differences in the development of liquid water path (LWP) in time and space. LWP is of key interest because it serves as a proxy for cloud production and has a high relevance to radiation (Sengupta et al., 2003). In the following discussion, x, y and z refer to the grid's west-east, south-north and vertical directions, respectively, and u, v and w refer to their respective velocity components.

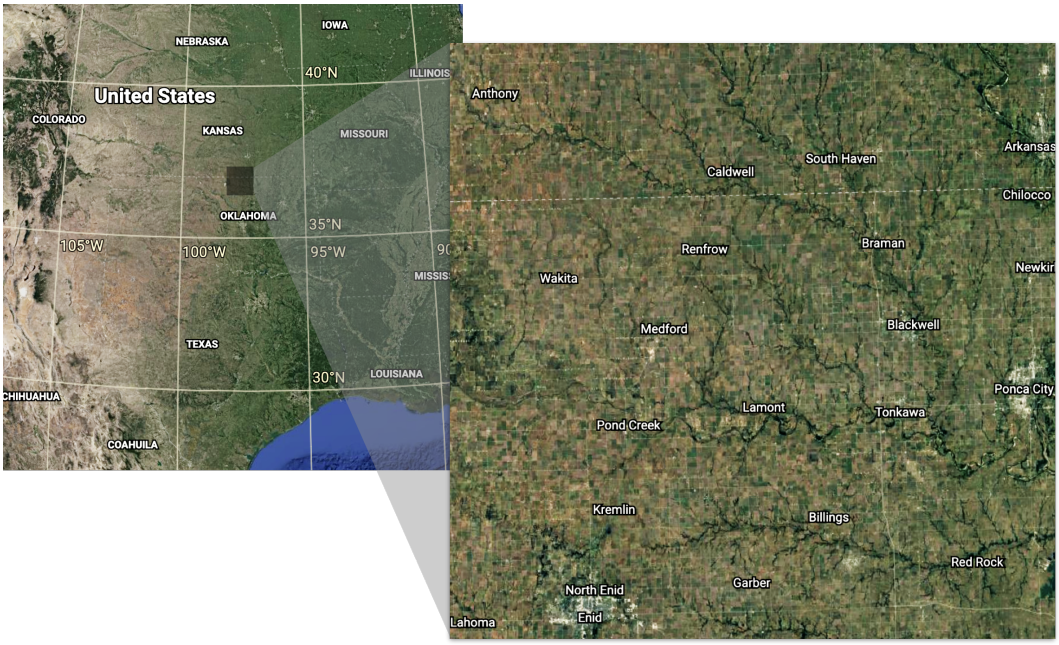

Figure 1. Map of the simulation domain, centered at the SGP site.

3.1 Heterogeneous vs. homogeneous

The primary day considered is September 24, 2017. This day was chosen due to the appreciable spatial heterogeneity in the LSM simulations. Following the LASSO setup, simulations are run for 15 hours beginning at 0538 LST (1200 UTC). Over the 100 km $\times$ 100 km domain, for both the heterogeneous and homogeneous simulations, the average sensible heat flux peaks at $t \approx 1030$ LST with a magnitude of approximately 215 W m^{-2}, and the domain-averaged latent heat flux peaks at the same time with a magnitude of approximately 130 W m^{-2} (Fig. 2a). In the heterogeneous case the standard deviations of the sensible and latent heat fluxes both peak at $t \approx 1230$ LST with values of approximately 40 and 45 W m^{-2}, respectively (Fig. 2b). Both simulations are initialized with the same domain-wide profiles for potential temperature, water vapor mixing ratio and lateral velocity components, shown in Fig. 3. The initial profile is stable with a water vapor mixing ratio of $\mathcal{O}(10$ g kg$^{-1})$ in the lower 4 km and a wind profile which is predominantly south-north with $v \approx 15$ m s^{-1} in the lower 10 km of the column.

Maps of the surface sensible heat flux and latent heat flux used to drive the WRF-LES surface, upscaled to $\Delta_{x,y} = 100$ m from the HydroBlocks output, are shown in Fig. 4 at $t = 1238$ LST, corresponding to the peak standard deviations for sensible and latent heat fluxes in the diurnal cycle. This day was chosen for the large moist patch in

the east of the domain, which is a result of scattered thunderstorms that occurred a few days before. Surface fields in the LES are specified from HydroBlocks every hour on the hour and are linearly interpolated in time at each timestep in between. The homogeneous case specifies the domain-averaged value of the aforementioned surface fields at each grid point, calculated at each timestep.

The heterogeneous and homogeneous simulations show a notable difference in both domain-wide LWP (Fig. 5a) and vertically-integrated, mass-coupled TKE (Fig. 5b) in time. Both cases begin to produce liquid water in the atmosphere at $t \approx 0930$ LST, but the two cases diverge at $t \approx 1130$ LST. The heterogeneous case continues to produce liquid water more rapidly, reaching a peak of nearly 300 g m^{-2} just before $t = 1400$ LST, while the homogeneous case has a lower rate of production, reaching a peak of ~ 250 g m^{-2} also near 1400 LST. Production of TKE between the two cases shows even larger differences, where the two cases diverge again at $t \approx 1130$ LST with the heterogeneous case reaching a much larger peak value than the homogeneous case.

To examine differences in spatial liquid water production, a map of each grid point's maximum LWP value throughout the duration of the simulation is shown for the heterogeneous (Fig. 6a) and homogeneous (Fig. 6b) cases. The heterogeneous case shows a very strong pattern of high liquid water production in the western half of the domain and low liquid water production in the eastern half of the domain, while the homogeneous case is more distributed throughout the center of the domain. Recalling that this case has a large moist patch in the east of the domain and a predominantly south-north flow, it appears that liquid water production for this case has a preference for areas with a high sensible heat flux at the surface, rather than areas with a high latent heat flux. We will see in Sec. 3.3 that the larger sensible heat fluxes alone are not sufficient to generate the levels of cloud production seen in the heterogeneous case, indicating that some circulation pattern potentially exists between the moist and dry areas of the domain; a phenomenon that has been observed in idealized modeling studies (e.g., Han et al., 2019).

Emergent mesoscale circulations in the heterogeneous case are examined with cross-section profiles of $u(x)$ at $t = 1408$ LST, approximately corresponding to the time of peak LWP in the domain, at $y = 45$ km (Fig. 7a) and averaged over the full domain in the y direction (Fig. 7b). The profiles reveal the anticipated general circulation behavior, where flow is primarily westward in the lower 2 km of the domain with a coherent band of eastward flow aloft which reaches a height of $z \approx 5$ km at $x \approx 35$ km, gradually descending to $z \approx 3$ km over the eastern edge of the domain. Due to the periodic lateral boundary conditions, the lower end of this layer from the eastern edge is also present in the westernmost 20 km of the domain. Up- and downdrafts are largely averaged out in the y-averaged cross-section, but are much more visible in the $y = 45$ km cross-section where a large visible updraft forms at $x \approx 35$ km, directly beneath the high point of the band of eastward flow aloft.

The same cross-sections of u are shown for the homogeneous case in (Fig. 8). The $y = 45$ km cross-section for the homogeneous case (Fig. 8a) does show many clear upwelling events, but they appear to dissipate in a few kilometers without developing any coherent circulation pattern, as is expected of an atmosphere with a uniform surface heating. The y-averaged cross-section for the homogeneous case (Fig. 8b) does have a band of eastward flow at $z \approx 4$ km, but its magnitude is much lower than in the heterogeneous case, and much of the flow appears closer to stagnant. There is also a strong westward flow in the lower 2 km of the homogeneous case, but without any clear pattern of upwelling anywhere in the domain. Unlike in the heterogeneous case, both bands in the homogeneous case span the full length of the domain in x.

Similar cross-section profiles across x of relative humidity and cloud mixing ratio domain-averaged in y, shown for the heterogeneous case in Figs. 7c, d and the homogeneous case at in Figs. 8c, d, respectively, further inform on the differences between the

two simulations, largely confirming what is already seen. The heterogeneous case has a very non-uniform profile of relative humidity in the x cross-section with well-mixed values reaching $z \approx 5$ km in the westernmost ~ 40 km of the domain, which appear to also pass through the periodic lateral boundary into the easternmost ~ 10 km of the domain. In the center of the domain the relative humidity reaches a maximum height of $z \approx 4$ km. Cloud production in the heterogeneous case is similarly focused in the west of the domain reaching an average cloud top above $z = 6$ km, with some sparser and lower clouds in the east of the domain that appear to have advected across the boundary from the western edge of the domain. The homogeneous case, conversely and expectedly, shows a very uniform mixing of relative humidity with the well-mixed layer reaching a height $z \approx 5$ km everywhere in the x cross-section. Cloud production in the homogeneous case is also very uniform across the domain, producing very sparse clouds compared to the heterogeneous simulation with a cloud top also at $z \approx 5$ km.

Compared to the homogeneous case, liquid water production in the heterogeneous case appears to benefit from both the moist and dry patches in its surface forcing, despite them not being co-located, via the latent heat flux from the moist patch being transported laterally to drier areas with a higher sensible heat flux which then lifts the moist air past the lifted condensation level resulting in local cloud production. The homogeneous case, which has the same domain-wide total surface latent and sensible heat fluxes, is unable to generate the same cloud production without local areas of higher sensible heat flux to produce similar local updrafts for the moisture that is present in the boundary layer. The following sections will further investigate the mechanisms driving the behavior of the heterogeneous case seen here.

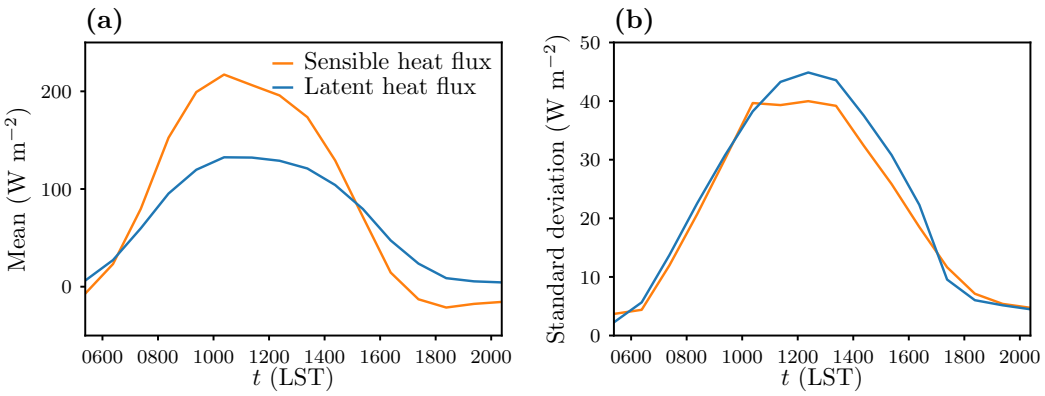

Figure 2. Time series of the surface sensible heat and latent heat fluxes used for the September 24, 2017 simulations: (a) domain mean for heterogeneous and homogeneous cases, (b) standard deviation for the heterogeneous case.

3.2 Land-surface components

The heterogeneity in the surface fields used in Sec. 3.1 is the result of four primary sources in the HydroBlocks model: river routing and subsurface flow, soil type, land cover, and forcing meteorology. To better understand the role of land-surface heterogeneity in atmospheric dynamics we present four additional WRF simulations which use surface maps from HydroBlocks when considering only certain sources of heterogeneity. The first simulation (the "R" case) contains surface heterogeneity generated only by rivers and subsurface flow, using surface fields from a HydroBlocks simulation which calculates river routing and subsurface flow as normal but uses homogenized fields for soil type, land cover, and forcing meteorology. The second simulation ("R+S") follows the same methodol-

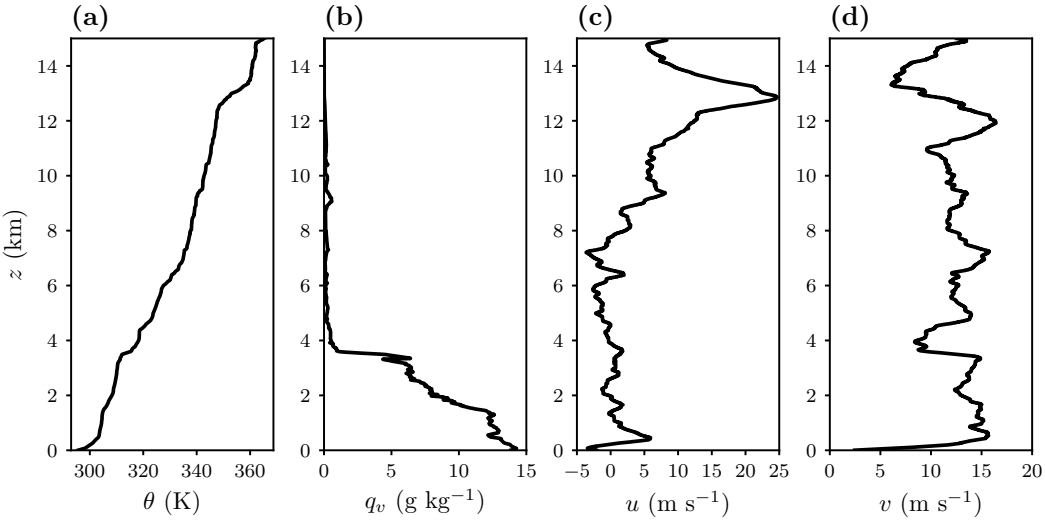

Figure 3. Initial profiles used for the September 24, 2017 simulations: (a) potential temperature, (b) water vapor mixing ratio, (c) u-velocity, (d) v-velocity.

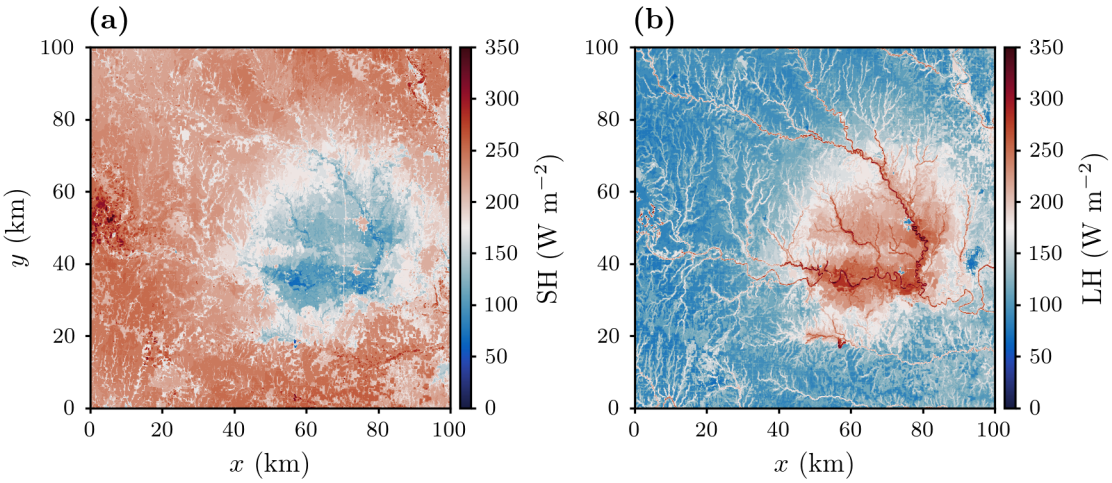

Figure 4. Heterogeneous surface values for the September 24, 2017 simulations at t = 1238 LST, upscaled from HydroBlocks: (a) sensible heat flux, (b) latent heat flux.

ogy but the driving HydroBlocks simulation also uses the heterogeneous soil-type map. The third simulation ("R+S+LC") uses the heterogeneous land cover field in addition to rivers/subsurface flow and soil type. The fourth simulation ("M") isolates surface heterogeneity generated by the meteorology driving the LSM by homogenizing the other fields. Each case is energetically constrained so that the domain-averaged surface sensible and latent heat fluxes remain unchanged from the base cases, thus only the standard deviations and spatial scales of heterogeneity differ between these four cases and those in Sec. 3.1. The fully heterogeneous case from Sec. 3.1 is equivalent to an "R+S+LC+M" case and is used here, along with its corresponding fully homogeneous case, as a reference for comparison.

Standard deviations of surface sensible heat flux and latent heat flux in time are shown in Fig. 9a, b, respectively. The sensible heat flux standard deviations are, very

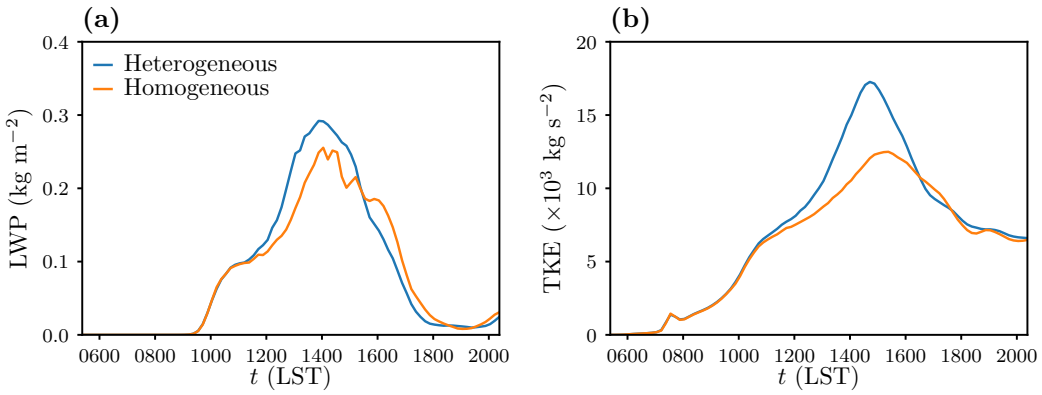

Figure 5. Domain-wide fields in time from the heterogeneous and homogeneous September 24, 2017 simulations: (a) LWP, (b) vertically integrated, mass-coupled TKE.

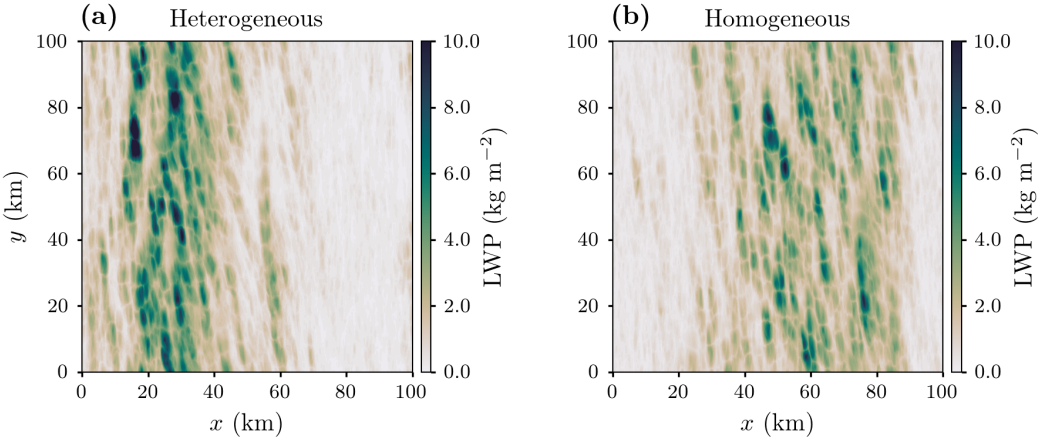

Figure 6. Maximum values of LWP at each grid point throughout the duration of the September 24, 2017 simulations using: (a) heterogeneous land surfaces, (b) homogeneous land surfaces.

approximately, linearly distributed with the R case peaking at the lowest value (approximately 10 W m^{-2}), followed by the R+S and R+S+LC cases. The M case has a peak standard deviation just below the fully heterogeneous case's peak value (approximately 40 W m^{-2}). The latent heat flux standard deviations, on the other hand, have two clear groups: the R, R+S, and R+S+LC cases which have peak values from approximately 10 to 20 W m^{-2}, and the fully heterogeneous and M cases which are nearly overlapping with a peak value of approximately 45 W m^{-2}.

Maps of surface sensible heat flux and latent heat flux at $t = 1238$ LST for the four cases are shown in Fig. 10. The R case has a largely homogeneous sensible heat flux field (Fig. 10a1) and a river network visible in the latent heat flux field (Fig. 10b1) which, despite appearing very heterogeneous, contains only small spatial scales of heterogeneity and spans the entire domain. The R+S case has a small visual increase in sensible and latent heat flux heterogeneity compared to the R case (Fig. 10a2, b2, respectively). The R+S+LC case adds considerable visual detail to the sensible heat flux (Fig. 10a3) and latent heat flux (Fig. 10b3) fields compared to the R+S case. The M case is largely homogeneous in both fields (Fig. 10a4, b4) aside from the $\mathcal{O}(50$ km) moist patch in the

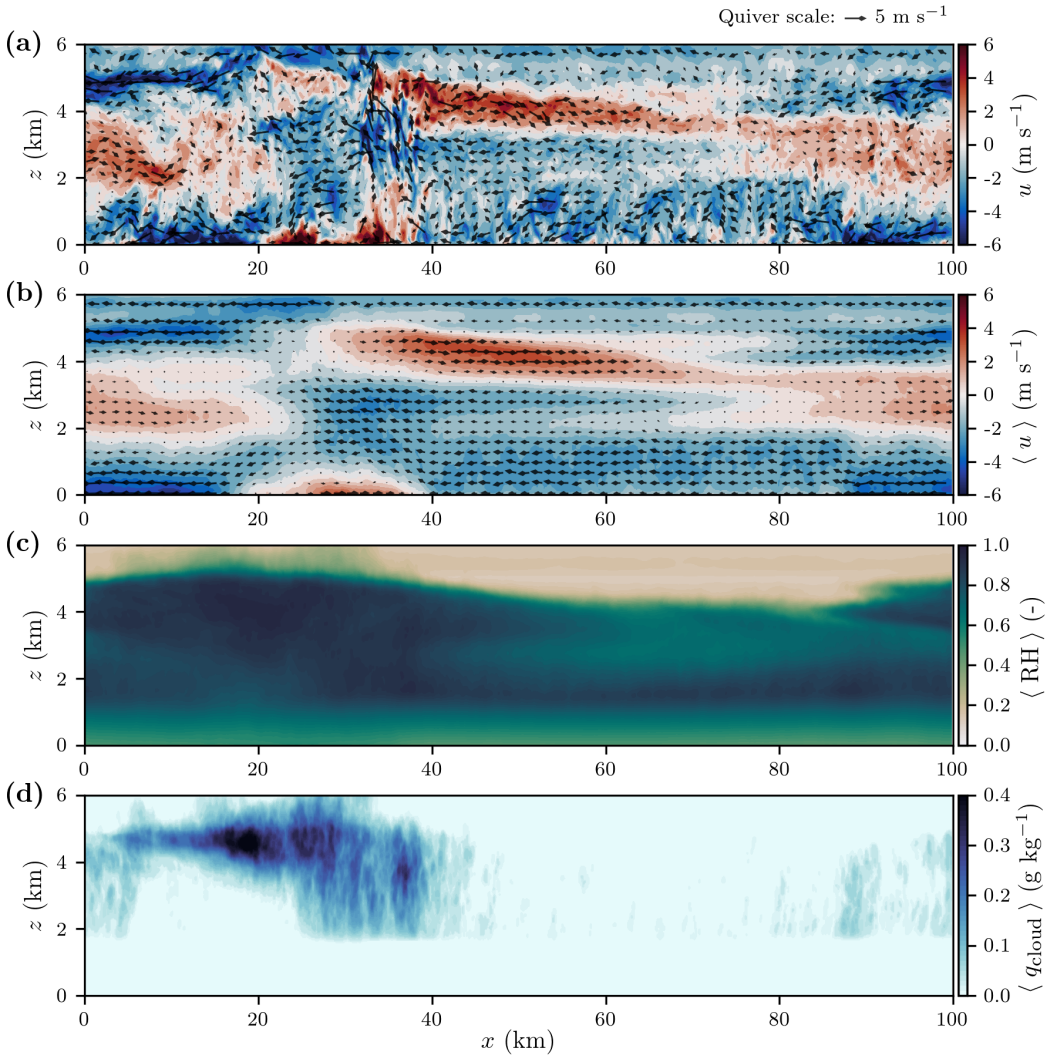

Figure 7. Profiles from the September 24, 2017 simulation using heterogeneous surfaces at t = 1408 LST of: (a) u-velocity along x at y = 45 km, (b) u-velocity along x and domain-averaged in y, (c) relative humidity along x and domain-averaged in y, (d) cloud mixing ratio along x and domain-averaged in y.

east of the domain, confirming that heterogeneous forcing meteorology is responsible for the larger scales of land-surface heterogeneity seen in the fully heterogeneous case.

Considering the resulting time series of LWP and TKE for these cases (Fig. 11a, b, respectively), the R and R+S cases are nearly indistinguishable from the fully homogeneous case while the R+S+LC case follows the fully homogeneous case until $t \approx 1330$ LST but then has a larger peak than the homogeneous case for both LWP and TKE. The M case produces liquid water and TKE very similarly to the fully heterogeneous case, where both diverge from the other cases at $t \approx 1130$ LST with similar production rates. The M case produces a slightly larger peak in LWP than the fully heterogeneous case, while the TKE production is nearly identical between the two. The M case produces nearly all of its liquid water in the westernmost 40 km of the domain while the other three cases are relatively homogeneous (not shown).

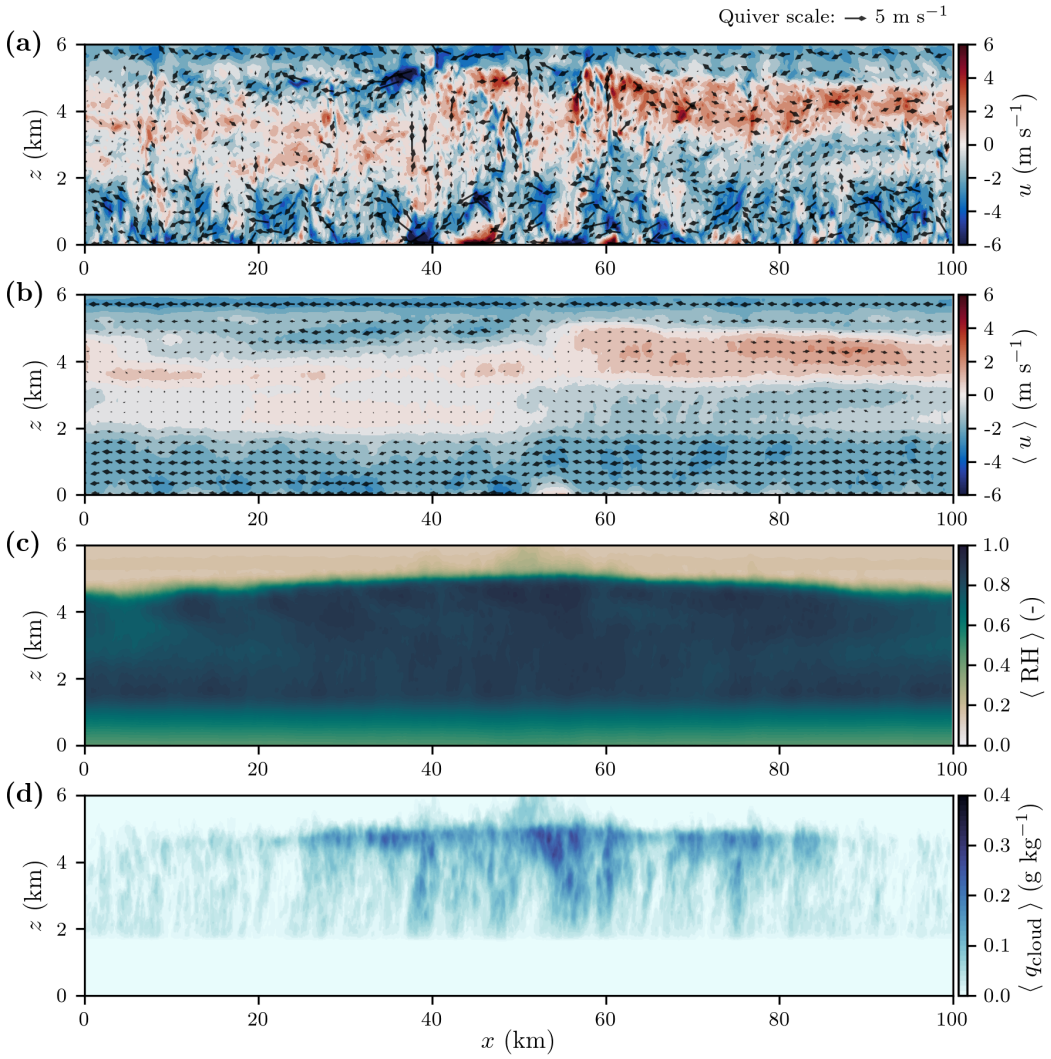

Figure 8. Profiles from the September 24, 2017 simulation using homogeneous surfaces at $t = 1408$ LST of: (a) u-velocity along x at $y = 45$ km, (b) u-velocity along x and domain-averaged in y, (c) relative humidity along x and domain-averaged in y, (d) cloud mixing ratio along x and domain-averaged in y.

It is seen that heterogeneous meteorology in the LSM is the primary driver of atmospherically-relevant heterogeneity in the land surface, even in the presence of a relatively strong wind profile as used here. While this seems trivial, land-surface heterogeneity is often traditionally seen as unimportant in the presence of even moderate winds as it will be "blended out" in the atmospheric boundary layer. It is also seen that the standard deviation of surface heterogeneity alone is insufficient to describe its impact on atmospheric dynamics, as demonstrated by the close agreement in LWP and TKE production between the fully homogeneous, R, and R+S cases despite significant differences in standard deviations.

3.3 Modified Bowen ratio and wind profile cases

It is proposed in Sec. 3.1 that the difference observed in cloud production between the heterogeneous and homogeneous cases is generated by emergent circulations between

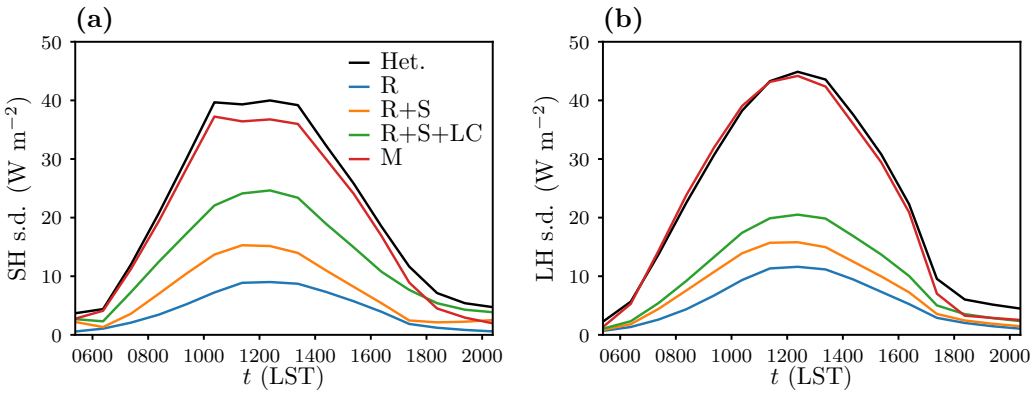

Figure 9. Time series of standard deviations of the surface fluxes used for the September 24, 2017 simulations where the land model includes heterogeneity from only rivers (R), rivers and soil type (R+S), rivers, soil type and land cover (R+S+LC), and only forcing meteorology (M): (a) sensible heat, (b) latent heat. The fully heterogeneous case is also shown for comparison.

the moist and dry areas of the land surface. However, it is also possible that the local areas of high sensible heat flux in the heterogeneous case are instead lifting the moisture that exists uniformly in the domain from the initial profile and large-scale forcing. To evaluate these two possible explanations, we consider heterogeneous cases with all of the surface latent heat flux at each grid point converted to additional sensible heat flux at the same grid point (the "0% latent heat" case) and 80% of the surface latent heat flux at each grid point converted to additional sensible heat flux at the same grid point (the "20% latent heat" case). Additionally, simulations in previous sections have all used the same initial wind profile, the consequence of which is unknown. To evaluate the effect of the wind profile, we consider a case with no wind in the initial profile (the "no wind" case) and a case where the wind at each vertical level of the initial profile is reoriented to be purely west-to-east (the "w-e wind" case). Both modified-wind cases use the unmodified heterogeneous land surface fields.

Time series of LWP and TKE for all four cases are shown in Fig. 12a, b, respectively. The increase in surface sensible heat flux in the 0% and 20% latent heat cases slightly speeds up the onset of liquid water production and significantly increases the TKE production in the first six hours compared to the fully heterogeneous and homogeneous cases. Both the 0% and 20% latent heat cases produce more liquid water in the first 8 hours of the simulation than the fully homogeneous case, but still less than the fully heterogeneous case once the heterogeneous case begins its high rate of production at $t \approx 1130$ LST. As well, the peak LWP values of both the 0% and 20% latent heat cases are very similar in magnitude to the fully homogeneous case. Both the 0% and 20% latent heat cases produce a large amount of TKE early but decline in their production rate after 1000 LST, and are thus ultimately surpassed by the fully heterogeneous case. Maps of maximum LWP throughout the simulation for the 0% and 20% latent heat cases show largely homogeneous liquid water production (not shown).

The results from the 0% and 20% latent heat cases give confidence that the presence of larger local sensible heat fluxes alone cannot explain the increase in liquid water production seen in the heterogeneous case compared to the homogeneous case. The results also imply that surface sensible heat flux drives the onset of TKE in the domain (for the same initial wind profile), which is also coupled to some degree to the initial liquid water production. This explains the agreement seen in previous sections until $t \approx$ 1130 LST, as all cases have the same domain-wide sensible heat flux and initial wind pro-

file. Perhaps the most interesting point to note is that in the 0% latent heat case any liquid water produced is solely from moisture that exists in the initial profile or that is introduced by the large-scale moisture flux forcing, both of which are applied uniformly in the domain. Still, the 0% latent heat case is able to produce liquid water at a rate initially faster than the fully homogeneous case or any case considered in Sec. 3.2, and reaches a peak LWP value that is nearly equal to the fully homogeneous case. The importance of the spatial structure of the Bowen ratio, implied by the similarities in cloud production between the homogeneous, 0% latent heat, and 20% latent heat cases, is especially interesting in the context of Qin et al. (2018), who found that the Bowen ratio is a significant factor in land-atmosphere coupling, particularly in the Southwestern United States, in a study on the added value of superparameterizations to precipitation in global climate models. These two results together continue to suggest that global ESMs could benefit from knowledge of SGS heterogeneity.

The liquid water production in the no wind case diverges from the heterogeneous and homogeneous cases just after 1030 LST and reaches a peak value larger than the base heterogeneous case approximately an hour earlier than the other cases. The TKE production in the no wind case begins development later than the heterogeneous and homogeneous cases, but develops very quickly once production begins, reaching a peak value approximately two hours earlier than the heterogeneous and homogeneous cases, with a magnitude very similar to the homogeneous case. The w-e wind case follows the base heterogeneous case very closely in both liquid water and TKE production, but shows a larger peak value in both fields with a similar timing.

Maps of maximum LWP at each grid point throughout the simulation for the two modified wind cases are particularly informative (Fig. 13). The no wind case (Fig. 13a) produces very concentrated individual clouds of a spatial scale $\mathcal{O}(1$ km) which themselves are very densely distributed in space (when considering the entire 15 hours together) over the entire dry portion of the domain, including the relatively small urban areas in the middle of the moist patch. The w-e wind case (Fig. 13b) shows a strong preference for liquid water production in the southern 30 km and northern 20 km of the domain, closely resembling the base heterogeneous case's aversion to cloud production over the moist patch but realigned to the w-e wind direction. The general spatial pattern of cloud production occurring over drier areas of the land surface is very similar to those seen in a highly idealized study by Avissar and Liu (1996).

The no wind and w-e wind cases show a very visible preference for cloud development over the dry (and thus, warm) areas of the land surface compared to the moist (and cool) areas, and also add context to the pattern seen for the base heterogeneous case in Fig. 6a. The behavior of the modified wind cases largely supports the explanation of circulations driving liquid water development in the heterogeneous case, which appears to occur in the cross-stream direction when there is a prevailing wind. The no wind case, which reaches its peak LWP earlier and with a larger magnitude than the base heterogeneous case, does lend some credence to the common wisdom that a mean wind will mix out surface heterogeneity. However, in addition to the differences between the base heterogeneous and homogeneous cases, the w-e wind case shows a larger peak LWP than either the base heterogeneous case or the no wind case, indicating that there are yet-uncovered subtleties in the relationship between surface heterogeneity and the wind profile. We also see in the no wind case that, while previous results indicate that LWP and TKE do show some relation, a larger (smaller) amount of TKE does not immediately suggest a larger (smaller) cloud production. Finally, the exaggerated response to land-surface heterogeneity seen in the no wind case eases potential concerns, to some degree, about the periodic lateral boundary conditions creating a positive feedback loop which amplifies the response of the atmosphere to heterogeneous surface fluxes.

3.4 Additional days

To justify the generality of the results seen here for September 24, 2017, two additional days at the SGP site are presented briefly for basic heterogeneous and homogeneous cases. These cases also use $\Delta_{x,y} = 100$ m, but are run on smaller 50 km $\times$ 50 km domains. Analysis for these cases is limited to time series of LWP.

Time series of domain-averaged surface sensible heat and latent heat fluxes for the two days are shown in Fig. 14. Compared to September 24, 2017 where the majority of the surface energy is in the sensible heat flux, June 10, 2016 has similar magnitudes of surface sensible and latent heat flux (Fig. 14a) while July 16, 2017 has a majority of its surface energy in its latent heat flux (Fig. 14b). Maps of the surface sensible and latent heat flux at $t = 1238$ LST for the two days are shown in Fig. 15. Both days have land surfaces which are dominated by rainfall from previous days, but in different patterns from each other and from September 24, 2017. The June 10, 2016 case has a surface pattern where moist patches are present in the north-east and south-west corners of the domain (Fig. 15a1, b1), while the moist patch in the July 16, 2017 case dominates the eastern two-thirds of the domain (Fig. 15a2, b2).

The time series of domain-wide LWP for heterogeneous and homogeneous simulations of both days (Fig. 16) show even more extreme behavior than the September 24, 2017 simulations, where the heterogeneous cases produce significantly more overall liquid water than their respective homogeneous cases, and with different patterns in time. While analysis of these two additional days has been very brief, the effect of land-surface heterogeneity on domain-wide LWP for these cases is seen to be even more significant than for the September 24, 2017 case. This confirmation inspires confidence in the notion that land-surface heterogeneity produced by previous heavy rain events can have a large influence on cloud production in the right conditions.

4 Discussion

The initial explanation, arrived at largely visually, that emergent mesoscale circulations between coherent moist and dry patches in the land surface are responsible for the the differences between the heterogeneous and homogeneous cases in Sec. 3.1 appears to gain credibility in the subsequent experiments. It is seen in Sec. 3.2 that the large moist and dry patches are indeed responsible for the observed cloud production in the heterogeneous case. In Sec. 3.3 it is seen that, while larger sensible heat fluxes do enhance cloud production compared to the base homogeneous case, the increased cloud production in the heterogeneous case cannot be fully explained by the case's larger local sensible heat fluxes alone.

It can be seen in Fig. 11 that the two cases which are forced by the LSM which includes heterogeneous forcing meteorology (the heterogeneous and M cases) diverge from the other four cases in both their liquid water and TKE production at $t \approx 1130$ LST. If our proposition that this divergence in behaviors is caused by the onset of an emergent mesoscale circulation is correct, then we should expect to see no visible circulation pattern in the velocity fields of the heterogeneous case at $t \approx 1030$ LST, and subtle beginnings of the pattern seen in Fig. 7 at $t \approx 1230$ LST. To this end, Fig. 17 shows cross-sections of u in the x-direction for the heterogeneous case at $t = 1038$ LST and $t = 1238$ LST, i.e. just before and after the proposed triggering of mesoscale circulations. When $t = 1038$ LST, there is no visible circulation pattern in either the y-averaged u field (Fig. 17a) or in the individual cross-section of u taken at $y = 45$ km (Fig. 17b). At $t = 1238$ LST, however, the circulation pattern is clearly visible in both the y-averaged (Fig. 17c) and $y = 45$ km (Fig. 17d) cross-sections of u, with a band of strong positive u spanning from $x \approx 20$ km to $x \approx 80$ km at a height of $z \approx 4$ km with a corresponding band of strong negative u spanning the same range in x in the lower 2 km of the at-

mosphere. The velocity in the column between the two layers has become nearly quiescent on average by 1238 LST and the beginnings of an emerging updraft can be seen at $x \approx 35$ km.

From the results seen here and in previous sections, it seems likely that both the magnitude and spatial scale of both land-surface and atmospheric heterogeneity, and the coupling between them, are important to understanding the dynamics of local cloud production, at least in certain cases. An interesting potential result is then that climate models, which currently run on grids which are still largely $\mathcal{O}(100$ km), should not only include considerations for SGS land-surface heterogeneity and mesoscale atmospheric circulations in their current cloud and turbulence parameterizations, but will find themselves in a still challenging situation when grids get closer to $\mathcal{O}(10$ km), where the relevant scales of land-surface heterogeneity and the associated meoscale circulations are similar to the grid scale, and thus cannot be fully resolved on the grid nor fully represented in an SGS parameterization. This situation is reminiscent of the "gray zone" problems seen in both the turbulence (Wyngaard, 2004) and cloud-modeling (Arakawa & Wu, 2013) communities. As such, barring a meteoric leap in computing capabilities, it is possible that representing land-surface heterogeneity will be an active and increasingly important issue for climate models for the foreseeable future. While the study here focuses primarily on cloud production, the impact of land-surface heterogeneity on the overall Earth system is not isolated to convection. For example, it is suggested by Mendes and Prevedello (2020), based on analysis of satellite observations, that secondary circulations between patches of different vegetation types has a cooling effect on surface temperatures.

The LES experiments presented here are an initial investigation into the effects of realistic land-surface and atmospheric heterogeneity, and are intended to be built upon with the ultimate goal of providing useful numerical data for climate-scale diagnostic and parameterization development. The land-surface fields used to drive the LESs are from a diurnal cycle in a spun-up and fully functional LSM using real datasets for land cover, soil type, surface-routing terrain, and meteorology. The fields from the LSM are also assimilated with the observationally-improved VARANAL dataset, further ensuring realistic energetics in the land surface. The spatial resolution and domain size are both also significant, with $\Delta_{x,y} = 100$ m over the 100 km $\times$ 100 km domain and $\Delta_z = 30$ m in the lower 5 km of the vertical column. In this regard, the simulations conducted here offer a significant and novel increase in realism towards the study of the coupling between land and atmosphere heterogeneity in an ESM. However, there are still many idealizations made in the simulations presented which warrant mentioning and examining further in future studies. The two most notable idealizations used here are: the semi-coupled LSM, where the land surface fields are specified *a priori* and do not receive feedback from the atmosphere as it is simulated, and, the periodic lateral boundary conditions.

The lack of a feedback between the atmosphere and the land surface means that clouds that develop do not influence the surface below. In particular, in these simulations clouds do not impact the local radiation budget of the land surface, which is one of the primary mechanisms of feedback from clouds to the land surface in the Earth system. The nature of coupling between clouds and surface radiation is generally a negative feedback, where the presence of clouds reduces the radiation budget at the surface. Considering that the primary conclusion from the semi-coupled simulations here is that clouds develop over areas of high surface sensible heat flux, the inclusion of atmospheric feedback to the land surface could potentially have a large reductive impact on the results seen here by reducing the local sensible heat flux once cloud production begins. Such a reduction could, in turn, have a damping effect on the generation of the mesoscale circulations observed here, which develop between dry and moist areas of the land surface. Future simulations which use a fully-coupled land surface, where the atmosphere can provide online feedback to the LSM, are currently under development by the co-authors and

will provide valuable insights into both the model requirements for an LES with highly heterogeneous land-surface fields and the degree of feedback from atmospheric heterogeneity to the land surface from a physical (though numerical) perspective.

The periodic lateral boundary conditions used in the simulations, while standard practice for LES and cloud-resolving studies, is another concession which potentially influences the results seen here. The cloud production in the no wind case in Sec. 3.3 shows a significant temporal and spatial response to land-surface heterogeneity with a very visible preference for production over drier areas of the land surface. It can thus be assumed that the observed results in the cases with wind are not reliant on the more numerical consequences of periodic lateral boundaries, for example the continual recycling of moist air across the domain. However, it is not clear how dependent the results are on the sustained fetches of high sensible heat adjacent to high latent heat that are created by the periodic boundaries. The 100 km $\times$ 100 km domain used for the September 24, 2017 cases is large enough to fully encapsulate the moist patch in the land surface, but, while it is plausible to imagine, it cannot be assumed that similar patterns are repeated over the surrounding landscape. In conjunction with the fully-coupled simulations mentioned above, nested simulations are also being developed to investigate the influence of the periodic lateral boundary conditions used here.

It should also be mentioned that, while $\Delta_{x,y} = 100$ m is a very high resolution in the cloud-resolving arena, the horizontal resolution does present another potential source for improvement. Multiple idealized studies of the so-called gray zone as it relates to resolving the ABL in an LES have found $\Delta_{x,y} = 100$ m to be a sufficient horizontal resolution while $\Delta_{x,y} = 200$ m begins to show signs of grid-dependent turbulence development (e.g., Beare, 2014; Efstathiou & Beare, 2015; J. S. Simon et al., 2019). By this standard, the resolution used here is near, but within, the limits of LES. It is not immediately clear how directly these and other idealized gray zone studies, which typically use uniform and constant surface sensible heat fluxes, translate to more realistic surface fluxes. In the simulations here, there is a small but noticeable burst of resolved TKE at $t \approx 0730$ LST in most of the cases (e.g., Fig. 5b), which is a common characteristic of an artificially delayed onset of resolved turbulence due to excessive horizontal dissipation of momentum and diffusion of heat from the turbulence closure model. Such an artifact in the early morning spin-up of the atmosphere does not necessarily indicate that the resolution is irredeemably coarse, so long as the delay of resolved turbulence is not significant and the overall dynamics are accurately simulated once turbulence is triggered. While the effect of the resolution seen here does not appear to be excessive, and the fields produced here certainly appear well-resolved, particularly the cross-sections of cloud mixing ratio in Figs. 7d and 8d, the effects of the horizontal resolution cannot fully be appreciated without comparison to even finer, as well as coarser, simulations of the same case. Such a study is currently under development and is anticipated to provide novel insights towards understanding land and atmosphere heterogeneity, as well as the gray zone of LES turbulence closure models in general.

Planned future work generally falls into one or both of two categories: clarifying the impact of different aspects of the LES configuration on cases with heterogeneous land surfaces, and, providing value to ongoing efforts towards diagnosing and modeling SGS heterogeneity in ESM parameterizations. On the clarification side, the aforementioned three studies (semi- vs. fully-coupled land surfaces, periodic vs. nested lateral boundary conditions, and an expanded range of horizontal resolutions) are the top priorities in the near future. Related to aiding diagnostic and parameterization efforts, the most immediate future work is focused on running heterogeneous and homogeneous simulations for multiple dozen additional days, with various initial conditions on the surface and in the atmosphere, at the SGP site aided by the available data from the LASSO campaign. In the longer term, we plan to extend simulations to additional locations around the globe where different forms of surface heterogeneity may be studied, e.g., lakes, moun-

tainous terrain, urban areas. These future studies are not exclusive efforts but will be conducted in conjunction with each other, i.e., model configuration choices will be tested for different days and locations, and knowledge gained regarding model behavior will be applied to the diagnostic and parameterization efforts when useful.

5 Summary and conclusions

Realistic land-surface fields are used to evaluate the role of land-surface heterogeneity on atmospheric dynamics by using high-resolution output from the HydroBlocks LSM to specify spatially heterogeneous and time-evolving surface conditions for sensible heat flux, latent heat flux, temperature (via emissivity and upward longwave radiation), albedo, and roughness coefficient in the WRF model, which is then run as a high-resolution LES over the SGP site in a variety of experiments. The primary experiment (Sec. 3.1) compares two simulations of the diurnal cycle on September 24, 2017: the first using the aforementioned heterogeneous surface fields and the second using time-evolving but spatially homogeneous surface fields, which take their uniform value of each field as the domain-average of the field in the heterogeneous case. It is observed that the heterogeneous case produces clouds more actively than the homogeneous case and in a spatial pattern that is correlated to the surface sensible heat flux fields. An explanation is offered that the heterogeneous simulation develops a circulation pattern between moist and dry areas where moist air originating over areas of high surface latent heat flux are transported laterally within the boundary layer to areas of high surface sensible heat flux, and are then lifted upwards through the boundary layer leading to cloud production.

Three sets of experiments which consider different modifications to the heterogeneous simulation are then presented, designed to elucidate the atmospheric dynamics generated by the heterogeneous land surface. The first set of modifications creates land surfaces which include only certain aspects of heterogeneity (Sec. 3.2). The second set of modifications increases the Bowen ratio in the heterogeneous case by converting local latent heat fluxes to sensible heat fluxes (Sec. 3.3). The final set of modifications uses the fully heterogeneous surfaces but adjusts the initial wind profile (Sec. 3.3). It is generally found that while there are many ways to produce more clouds and TKE than the fully homogeneous case, it is much more difficult to match the peak magnitude of cloud production seen in the heterogeneous case without the mesoscale patterns created in the surface heat fluxes by forcing the LSM with heterogeneous meteorology fields. The lack of similarity between cloud production in the base heterogeneous case and the cases with increased Bowen ratios shows that the areas with above-average sensible heat flux alone are not the source of the increased production, but that the remote latent heat fluxes are also necessary. We also see that re-orienting the prevailing wind in the atmosphere will correspondingly re-orient the cloud-production pattern to remain focused over the dry areas, and that removing the mean wind entirely allows clouds to form everywhere that is associated with a high surface sensible heat flux.

The last set of additional experiments is a brief analysis of two other summer days at the SGP site, both also with large, but unique, scales of spatial heterogeneity generated by scattered storms at the site on previous days (Sec. 3.4). Of the two additional days shown, the surface energy fluxes on June 10, 2016 are relatively evenly distributed between latent and sensible heat and the surface energy fluxes on July 16, 2017 are predominantly in the form of latent heat, providing complements to the primary September 24, 2017 case, where surface energy fluxes are predominantly in the form of sensible heat. Both additional days show a significantly larger domain-wide LWP values in the heterogeneous cases compared to their homogeneous counterparts.

Finally, a discussion of observations from the different experiments leads to further analysis and a bolstering of the mesoscale circulation explanation for the observed increase in cloud production seen in the heterogeneous case (Sec. 4). Potential shortcom-

674 ings of the simulations conducted for this study are also discussed, and future experi-
675 ments are outlined. While the analysis presented here is largely for a single day there
676 appears to be some generality to the conclusion that spatial heterogeneity of the land
677 surface plays a key role in cloud production. It follows that SGS cloud and turbulence
678 parameterizations for weather and climate models should also include information about
679 SGS land-surface heterogeneity and vice versa, though an effective mechanism to do so
680 is yet undeveloped. We hope that this and future work will aid in the development of
681 such mechanisms.

682 **Acknowledgments**
683 Funded by NOAA grant NA19OAR4310241. PD's contribution is funded by NOAA grant
684 NA19OAR4310242.

685 Data availability: Simulations here use a modification of WRF version 3.8.1 devel-
686 oped and maintained by the LASSO team. The base WRF code, initial sounding files,
687 and large-scale forcing files are available from W. Gustafson et al. (2019). Additional mod-
688 ifications to the WRF code to specify heterogeneous surfaces, data files for surface fields
689 for each simulation, and model control files for each simulation are available at J. Simon
690 and Chaney (2021).

691 References

692 Albertson, J. D., Kustas, W. P., & Scanlon, T. M. (2001). Large-eddy simulation
693 over heterogeneous terrain with remotely sensed land surface conditions. *Water*
694 *Resources Research*, *37*(7), 1939–1953.
695 Arakawa, A., & Wu, C.-M. (2013). A unified representation of deep moist convection
696 in numerical modeling of the atmosphere. Part I. *J. Atmos. Sci.*, *70*(7), 1977–
697 1992. doi: 10.1175/JAS-D-12-0330.1
698 Avissar, R., & Liu, Y. (1996). Three-dimensional numerical study of shallow convec-
699 tive clouds and precipitation induced by land surface forcing. *Journal of Geo-*
700 *physical Research: Atmospheres*, *101*(D3), 7499–7518.
701 Avissar, R., & Schmidt, T. (1998). An Evaluation of the Scale at which Ground-
702 Surface Heat Flux Patchiness Affects the Convective Boundary Layer Using
703 Large-Eddy Simulations. *Journal of the Atmospheric Sciences*, *55*(16), 2666-
704 2689. Retrieved from `https://doi.org/10.1175/1520-0469(1998)055<2666:`
705 `AEOTSA>2.0.CO;2` doi: 10.1175/1520-0469(1998)055⟨2666:AEOTSA⟩2.0.CO;
706 2
707 Beare, R. J. (2014). A length scale defining partially-resolved boundary-layer turbu-
708 lence simulations. *Boundary-Layer Meteorol.*, *151*(1), 39–55.
709 Bertoldi, G., Kustas, W. P., & Albertson, J. D. (2013). Evaluating source area
710 contributions from aircraft flux measurements over heterogeneous land using
711 large-eddy simulation. *Boundary-layer meteorology*, *147*(2), 261–279.
712 Bonan, G. B., Oleson, K. W., Vertenstein, M., Levis, S., Zeng, X., Dai, Y., ... Yang,
713 Z.-L. (2002). The land surface climatology of the Community Land Model
714 coupled to the NCAR Community Climate Model. *Journal of climate*, *15*(22),
715 3123–3149.
716 Bou-Zeid, E., Meneveau, C., & Parlange, M. B. (2004). Large-eddy simulation of
717 neutral atmospheric boundary layer flow over heterogeneous surfaces: Blending
718 height and effective surface roughness. *Water Resources Research*, *40*(2).
719 Chaney, N. W., Metcalfe, P., & Wood, E. F. (2016). HydroBlocks: a field-scale
720 resolving land surface model for application over continental extents. *Hydro-*
721 *logical Processes*, *30*(20), 3543-3559. Retrieved from `https://onlinelibrary`
722 `.wiley.com/doi/abs/10.1002/hyp.10891` doi: 10.1002/hyp.10891
723 Chaney, N. W., Minasny, B., Herman, J. D., Nauman, T. W., Brungard, C. W.,
724 Morgan, C. L., ... Yimam, Y. (2019). POLARIS soil properties: 30-m prob-

abilistic maps of soil properties over the contiguous United States. *Water Resources Research*, *55*(4), 2916–2938.

Chaney, N. W., Roundy, J. K., Herrera-Estrada, J. E., & Wood, E. F. (2015). High-resolution modeling of the spatial heterogeneity of soil moisture: Applications in network design. *Water Resources Research*, *51*(1), 619–638.

Chaney, N. W., Torres-Rojas, L., Vergopolan, N., & Fisher, C. K. (2020). Two-way coupling between the sub-grid land surface and river networks in Earth system models. *Geoscientific Model Development Discussions*, *2020*, 1–31. Retrieved from `https://gmd.copernicus.org/preprints/gmd-2020-291/` doi: 10.5194/gmd-2020-291

Chaney, N. W., Van Huijgevoort, M. H., Shevliakova, E., Malyshev, S., Milly, P. C., Gauthier, P. P., & Sulman, B. N. (2018). Harnessing big data to rethink land heterogeneity in Earth system models. *Hydrology and Earth System Sciences*, *22*(6), 3311–3330.

Chaney, N. W., Wood, E. F., McBratney, A. B., Hempel, J. W., Nauman, T. W., Brungard, C. W., & Odgers, N. P. (2016). POLARIS: A 30-meter probabilistic soil series map of the contiguous United States. *Geoderma*, *274*, 54–67.

Clark, M. P., Fan, Y., Lawrence, D. M., Adam, J. C., Bolster, D., Gochis, D. J., ... others (2015). Improving the representation of hydrologic processes in Earth System Models. *Water Resources Research*, *51*(8), 5929–5956.

Cosgrove, B. A., Lohmann, D., Mitchell, K. E., Houser, P. R., Wood, E. F., Schaake, J. C., ... others (2003). Real-time and retrospective forcing in the North American Land Data Assimilation System (NLDAS) project. *Journal of Geophysical Research: Atmospheres*, *108*(D22).

Ducharne, A., Koster, R. D., Suarez, M. J., Stieglitz, M., & Kumar, P. (2000). A catchment-based approach to modeling land surface processes in a general circulation model: 2. parameter estimation and model demonstration. *Journal of Geophysical Research: Atmospheres*, *105*(D20), 24823–24838.

Efstathiou, G., & Beare, R. J. (2015). Quantifying and improving sub-grid diffusion in the boundary-layer grey zone. *Q J R Meteorol Soc*, *141*(693), 3006–3017.

Findell, K. L., & Eltahir, E. A. (2003). Atmospheric controls on soil moisture-boundary layer interactions: Three-dimensional wind effects. *Journal of Geophysical Research: Atmospheres*, *108*(D8).

Golaz, J.-C., Larson, V. E., & Cotton, W. R. (2002). A PDF-based model for boundary layer clouds. Part I: Method and model description. *Journal of the atmospheric sciences*, *59*(24), 3540–3551.

Gómez-Plaza, A., Martınez-Mena, M., Albaladejo, J., & Castillo, V. (2001). Factors regulating spatial distribution of soil water content in small semiarid catchments. *Journal of hydrology*, *253*(1-4), 211–226.

Gustafson, W., Vogelmann, A., Cheng, X., Dumas, K., Endo, S., Johnson, K., ... Xiao, H. (2019). Description of the LASSO data bundles product. DOE Atmospheric Radiation Measurement (ARM) user facility. *DOE/SC-ARM-TR-216*. doi: 10.2172/1469590

Gustafson, W. I., Vogelmann, A. M., Li, Z., Cheng, X., Dumas, K. K., Endo, S., ... Xiao, H. (2020). The Large-eddy simulation (LES) Atmospheric Radiation Measurement (ARM) Symbiotic Simulation and Observation (LASSO) activity for continental shallow convection. *Bulletin of the American Meteorological Society*, *101*(4), E462–E479.

Gutowski, W. J., Ullrich, P. A., Hall, A., Leung, L. R., OBrien, T. A., Patricola, C. M., ... others (2020). The ongoing need for high-resolution regional climate models: Process understanding and stakeholder information. *Bulletin of the American Meteorological Society*, *101*(5), E664–E683.

Han, C., Brdar, S., Raasch, S., & Kollet, S. (2019). Large-eddy simulation of catchment-scale circulation. *Quarterly Journal of the Royal Meteorological Society*, *145*(720), 1218–1233.

Homer, C. H., Fry, J. A., & Barnes, C. A. (2012). The national land cover database. *US Geological Survey Fact Sheet*, *3020*(4), 1–4.

Huang, H.-Y., & Margulis, S. A. (2013). Impact of soil moisture heterogeneity length scale and gradients on daytime coupled land-cloudy boundary layer interactions. *Hydrological Processes*, *27*(14), 1988–2003.

Jacobs, J., Mohanty, B., Hsu, E., & Miller, D. (2004). Field scale variability and similarity of soil moisture. *Remote Sens. Environ*, *92*, 436–446.

Kang, S.-L. (2016). Regional Bowen ratio controls on afternoon moist convection: A large eddy simulation study. *Journal of Geophysical Research: Atmospheres*, *121*(23), 14,056-14,083. Retrieved from `https://agupubs.onlinelibrary.wiley.com/doi/abs/10.1002/2016JD025567` doi: 10.1002/2016JD025567

Kang, S.-L. (2020). Effects of mesoscale surface heterogeneity on the afternoon and early evening transition of the atmospheric boundary layer. *Boundary-Layer Meteorology*, *174*(3), 371–391.

Kustas, W. P., & Albertson, J. D. (2003). Effects of surface temperature contrast on land-atmosphere exchange: A case study from monsoon 90. *Water Resources Research*, *39*(6).

Lawrence, D. M., Fisher, R. A., Koven, C. D., Oleson, K. W., Swenson, S. C., Bonan, G., ... others (2019). The Community Land Model version 5: Description of new features, benchmarking, and impact of forcing uncertainty. *Journal of Advances in Modeling Earth Systems*, *11*(12), 4245–4287.

Lin, Y., & Mitchell, K. E. (2005). The NCEP stage II/IV hourly precipitation analyses: Development and applications. In *Proceedings of the 19th conference hydrology, american meteorological society, san diego, ca, usa* (Vol. 10).

Mendes, C. B., & Prevedello, J. A. (2020). Does habitat fragmentation affect landscape-level temperatures? A global analysis. *Landscape Ecology*, *35*(8), 1743–1756.

Milly, P. C., Malyshev, S. L., Shevliakova, E., Dunne, K. A., Findell, K. L., Gleeson, T., ... Swenson, S. (2014). An enhanced model of land water and energy for global hydrologic and earth-system studies. *Journal of Hydrometeorology*, *15*(5), 1739–1761.

Mitchell, K. E., Lohmann, D., Houser, P. R., Wood, E. F., Schaake, J. C., Robock, A., ... others (2004). The multi-institution North American Land Data Assimilation System (NLDAS): Utilizing multiple GCIP products and partners in a continental distributed hydrological modeling system. *Journal of Geophysical Research: Atmospheres*, *109*(D7).

Niu, G.-Y., Yang, Z.-L., Mitchell, K. E., Chen, F., Ek, M. B., Barlage, M., ... others (2011). The community Noah land surface model with multiparameterization options (Noah-MP): 1. model description and evaluation with local-scale measurements. *Journal of Geophysical Research: Atmospheres*, *116*(D12).

Ntelekos, A. A., Smith, J. A., Baeck, M. L., Krajewski, W. F., Miller, A. J., & Goska, R. (2008). Extreme hydrometeorological events and the urban environment: Dissecting the 7 july 2004 thunderstorm over the Baltimore MD Metropolitan Region. *Water Resources Research*, *44*(8).

Phillips, T. J., & Klein, S. A. (2014). Land-atmosphere coupling manifested in warm-season observations on the US southern great plains. *Journal of Geophysical Research: Atmospheres*, *119*(2), 509–528.

Pielke Sr, R. A. (2001). Influence of the spatial distribution of vegetation and soils on the prediction of cumulus convective rainfall. *Reviews of Geophysics*, *39*(2), 151–177.

Qin, H., Pritchard, M. S., Kooperman, G. J., & Parishani, H. (2018). Global effects of superparameterization on hydrothermal land-atmosphere coupling on multiple timescales. *Journal of Advances in Modeling Earth Systems*, *10*(2), 530–549.

Senatore, A., Mendicino, G., Gochis, D. J., Yu, W., Yates, D. N., & Kunstmann,

H. (2015). Fully coupled atmosphere-hydrology simulations for the central Mediterranean: Impact of enhanced hydrological parameterization for short and long time scales. *Journal of Advances in Modeling Earth Systems*, *7*(4), 1693–1715.

Sengupta, M., Clothiaux, E. E., Ackerman, T. P., Kato, S., & Min, Q. (2003). Importance of accurate liquid water path for estimation of solar radiation in warm boundary layer clouds: An observational study. *Journal of climate*, *16*(18), 2997–3009.

Shao, Y., Liu, S., Schween, J. H., & Crewell, S. (2013). Large-eddy atmosphere-land-surface modelling over heterogeneous surfaces: Model development and comparison with measurements. *Boundary-layer meteorology*, *148*(2), 333–356.

Shrestha, P., Sulis, M., Masbou, M., Kollet, S., & Simmer, C. (2014). A scale-consistent terrestrial systems modeling platform based on COSMO, CLM, and ParFlow. *Monthly weather review*, *142*(9), 3466–3483.

Simon, J., & Chaney, N. (2021, May). *Data for: Semi-coupling of a Field-scale Resolving Land-surface Model and WRF-LES to Investigate the Influence of Land-surface Heterogeneity on Cloud Development.* Zenodo. Retrieved from `https://doi.org/10.5281/zenodo.4741327` doi: 10.5281/zenodo.4741327

Simon, J. S., Zhou, B., Mirocha, J. D., & Chow, F. K. (2019). Explicit filtering and reconstruction to reduce grid dependence in convective boundary layer simulations using WRF-LES. *Mon Weather Rev*, *147*(5), 1805-1821. doi: 10.1175/MWR-D-18-0205.1

Skamarock, W., Klemp, J., Dudhia, J., Gill, D., Barker, D., Duda, M., ... Powers, J. (2008). A description of the Advanced Research WRF version 3. *NCAR Technical Note, NCAR/TN-475+STR*.

Sušelj, K., Teixeira, J., & Chung, D. (2013). A unified model for moist convective boundary layers based on a stochastic eddy-diffusivity/mass-flux parameterization. *Journal of the Atmospheric Sciences*, *70*(7), 1929–1953.

Talbot, C., Bou-Zeid, E., & Smith, J. (2012). Nested mesoscale large-eddy simulations with WRF: Performance in real test cases. *Journal of Hydrometeorology*, *13*(5), 1421–1441.

Taylor, C. M., de Jeu, R. A., Guichard, F., Harris, P. P., & Dorigo, W. A. (2012). Afternoon rain more likely over drier soils. *Nature*, *489*(7416), 423–426.

Taylor, C. M., Gounou, A., Guichard, F., Harris, P. P., Ellis, R. J., Couvreux, F., & De Kauwe, M. (2011). Frequency of Sahelian storm initiation enhanced over mesoscale soil-moisture patterns. *Nature Geoscience*, *4*(7), 430–433.

Timmermans, W., Bertoldi, G., Albertson, J., Olioso, A., Su, Z., & Gieske, A. (2008). Accounting for atmospheric boundary layer variability on flux estimation from rs observations. *International journal of remote sensing*, *29*(17-18), 5275–5290.

Vergopolan, N., Chaney, N. W., Beck, H. E., Pan, M., Sheffield, J., Chan, S., & Wood, E. F. (2020). Combining hyper-resolution land surface modeling with SMAP brightness temperatures to obtain 30-m soil moisture estimates. *Remote Sensing of Environment*, *242*, 111740.

Western, A. W., Grayson, R. B., Blöschl, G., Willgoose, G. R., & McMahon, T. A. (1999). Observed spatial organization of soil moisture and its relation to terrain indices. *Water resources research*, *35*(3), 797–810.

Wyngaard, J. C. (2004). Toward numerical modeling in the "terra incognita". *J. Atmos. Sci.*, *61*(14), 1816–1826. doi: 10.1175/1520-0469(2004)061⟨1816:TNMITT⟩2.0.CO;2

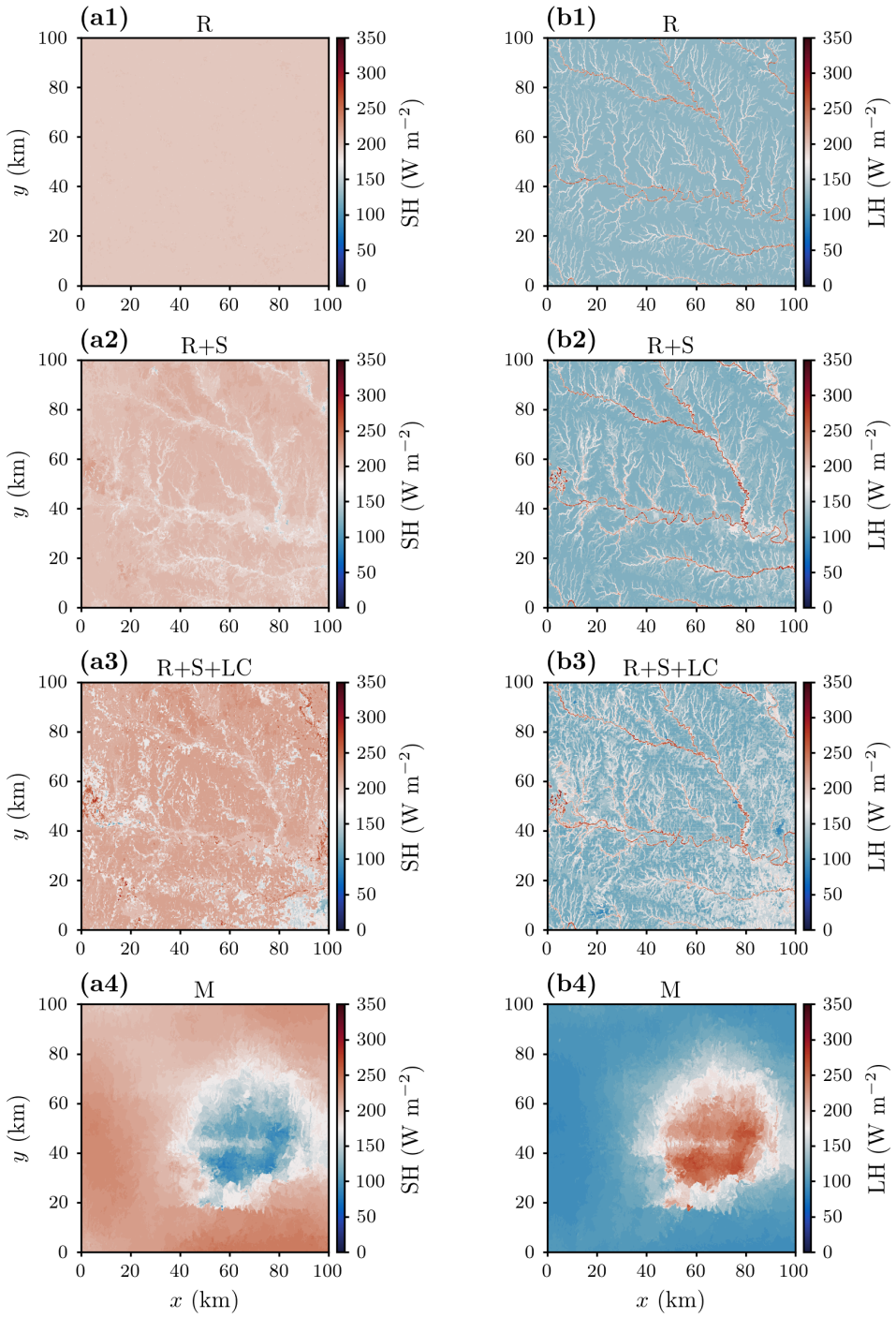

Figure 10. (column a) Surface sensible heat flux and (column b) latent heat flux fields for September 24, 2017 simulations at t = 1238 LST with land surfaces which include heterogeneity from: (row 1) only rivers (R), (row 2) rivers and soil type (R+S), (row 3) rivers, soil type and land cover (R+S+LC), and (row 4) only forcing meteorology (M).

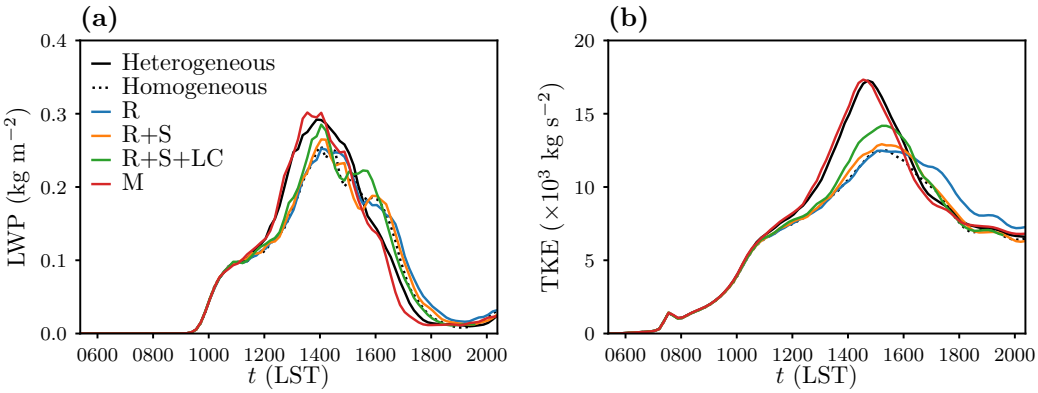

Figure 11. Domain-wide fields in time from the September 24, 2017 simulations where the land model includes heterogeneity from only rivers (R), rivers and soil type (R+S), rivers, soil type and land cover (R+S+LC), and only forcing meteorology (M): (a) LWP, (b) vertically integrated, mass-coupled TKE. The fully heterogeneous and fully homogeneous cases are also shown for comparison.

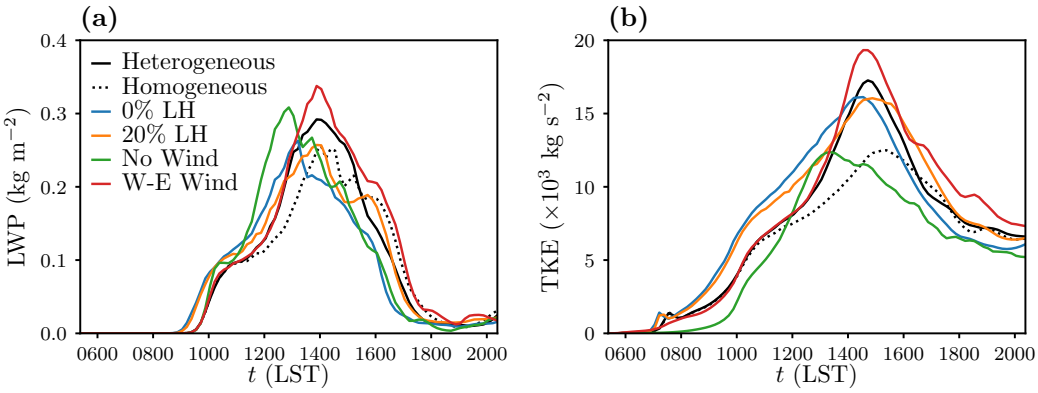

Figure 12. Domain-wide fields in time from the 0% LH, 20% LH, no wind, and w-e wind simulations of September 24, 2017: (a) LWP, (b) vertically integrated, mass-coupled TKE. The fully heterogeneous and fully homogeneous cases are also shown for comparison.

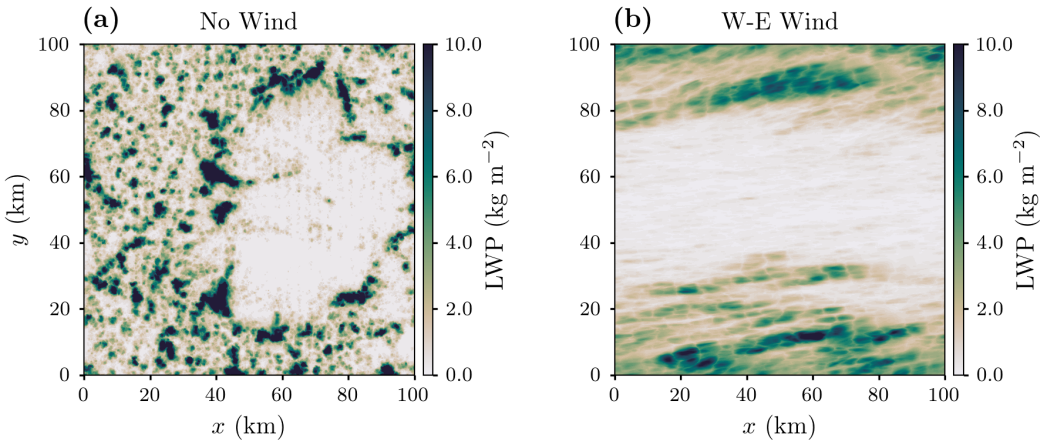

Figure 13. Maximum values of LWP at each grid point throughout the duration of September 24, 2017 simulations with different initial wind profiles: (a) modified to have zero initial mean wind in the column and (b) re-oriented to a purely west-east initial mean wind.

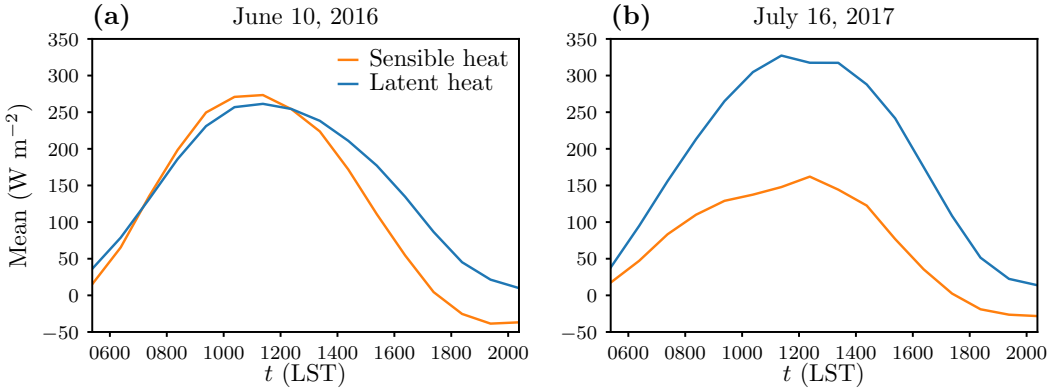

Figure 14. Time series of the domain mean surface sensible heat and latent heat fluxes used for simulations of: (a) June 10, 2016 and (b) July 16, 2017.

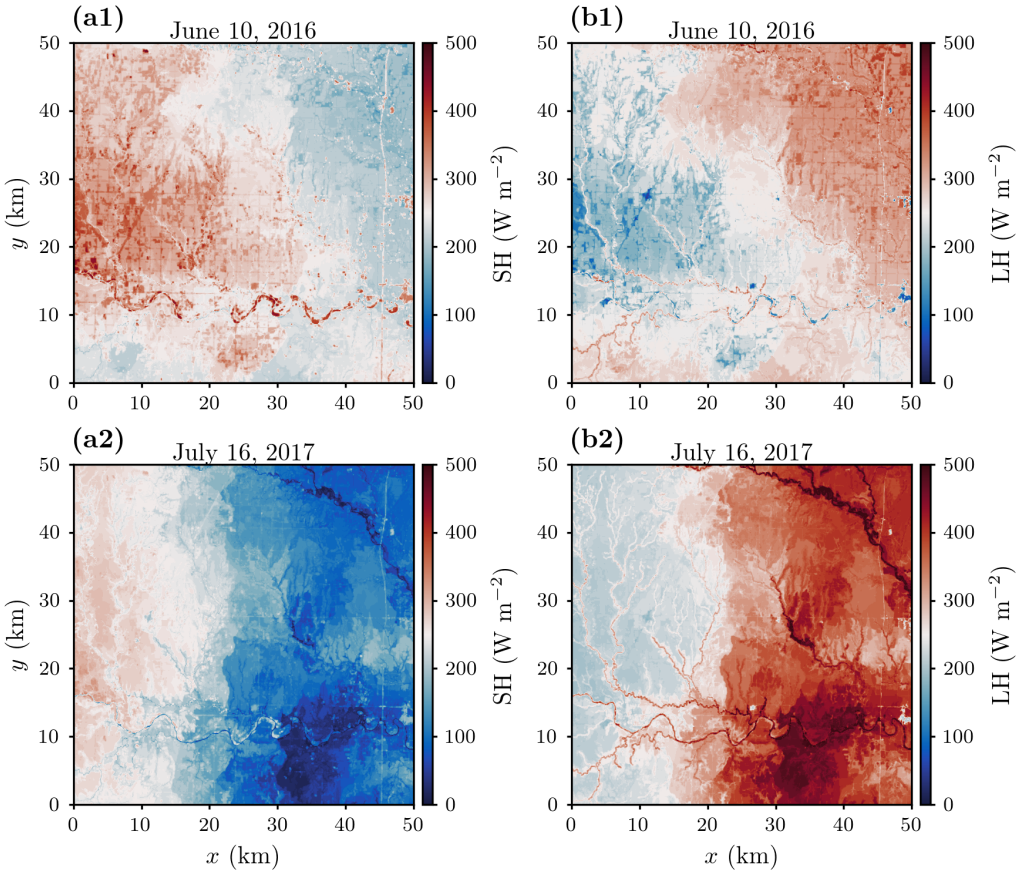

Figure 15. (column a) Surface sensible heat flux and (column b) latent heat flux fields at t = 1238 LST for simulations of: (row 1) June 10, 2016 and (row 2) July 16, 2017.

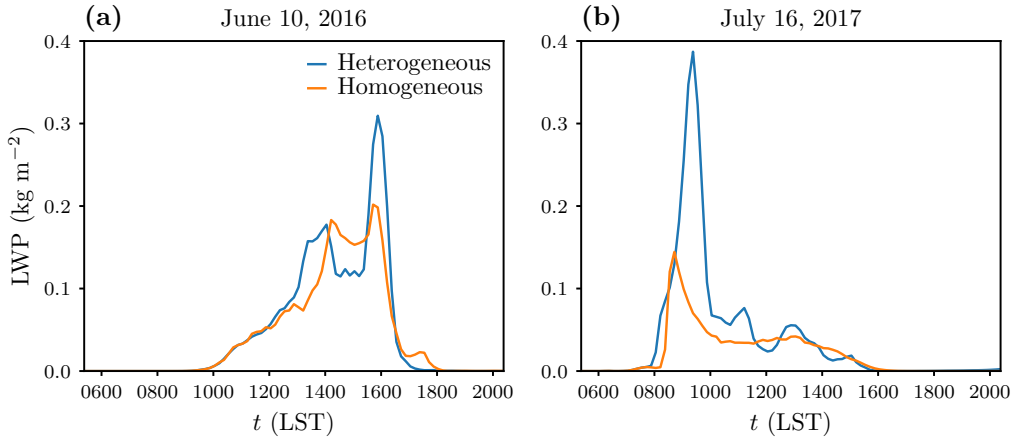

Figure 16. Domain-wide LWP in time from the heterogeneous and homogeneous simulations of: (a) June 10, 2016 and (b) July 16, 2017.

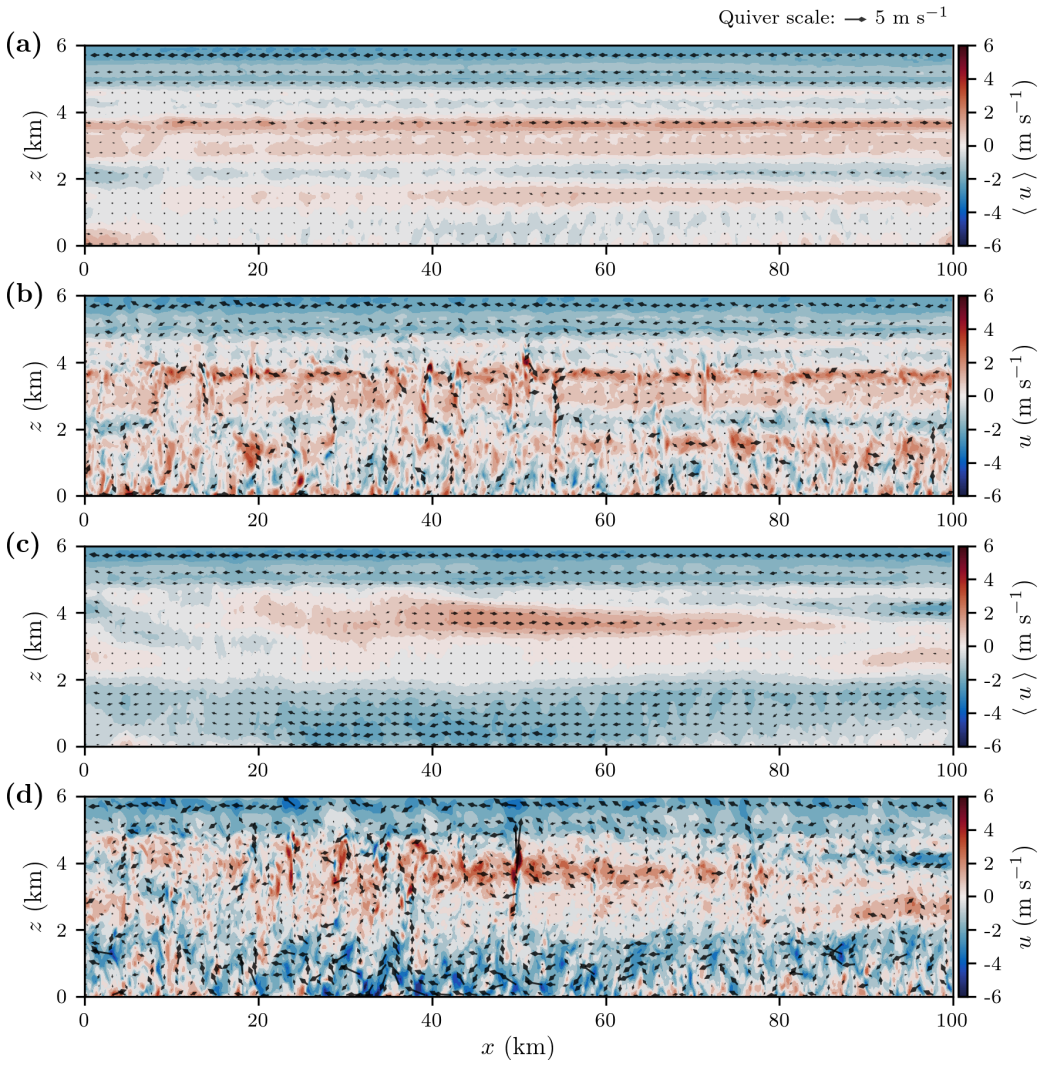

Figure 17. Profiles from the September 24, 2017 simulation using heterogeneous surfaces (from Sec. 3.1) of: (a) u-velocity along x and domain-averaged in y at t = 1038 LST, (b) u-velocity along x at y = 45 km and t = 1038 LST, (c) u-velocity along along x and domain-averaged in y at $t = 1238$ LST, (d) u-velocity along x at $y = 45$ km and $t = 1238$ LST.